**Proceedings of the ASME 2010 3rd Joint US-European Fluids Engineering Summer Meeting and
8th International Conference on Nanochannels, Microchannels, and Minichannels
FEDSM-ICNMM2010
August 1-5, 2010, Montreal, Canada**

FEDSM-ICNMM2010-' 0- ' -

A NUMERICAL METHOD FOR UNCERTAIN COMPRESSIBLE FLOWS

G. Poëtte

CEA/DAM/DIF
F-91297 Arpajon, France
Email: gael.poette@cea.fr

D. Lucor

Institut Jean Le Rond d'Alembert
UPMC, 4 place Jussieu,
75252, Paris cedex 05, France,
Email: didier.lucor@upmc.fr

B. Després

Laboratoire Jacques-Louis Lions,
UPMC, 4 place Jussieu,
75252, Paris cedex 05, France,
Email: despres@ann.jussieu.fr

ABSTRACT

The treatment of uncertain interface positions in complex simulations and the propagation of the latter uncertainty through complex systems is an important issue. In this paper, we tackle the characterization of perturbed interfaces between fluids thanks to stochastic modelization and the propagation of the initial uncertainty through the Euler system. The stochastic Euler system is solved applying Polynomial Chaos theory through the Intrusive Polynomial Moment Method (IPMM), see [23]. Numerical results are presented for several configurations of the uncertain interface. The system presents an important sensitivity with respect to the stochastic initially leading modes of the uncertain interface.

INTRODUCTION

In this paper, we are interested in quantifying uncertainties on interfaces between several materials: our motivation is *I*nertial *F*usion *C*onfinment (ICF), see figure 1 and [13]. Being able to treat uncertain interface positions in such complex simulations is an important issue: ICF consists in heating and compressing a fuel target in order to trigger nuclear fusion reactions. The energy is delivered to the outer layer of the target by high energy beams of laser light. The heated outer layer explodes outward and the reaction force accelerates the target inward sending shock waves to the center. If the set of shock wave is sufficiently powerful, the heating and compression at the center of the target is such that nuclear fusion reactions occur. The later description corre-
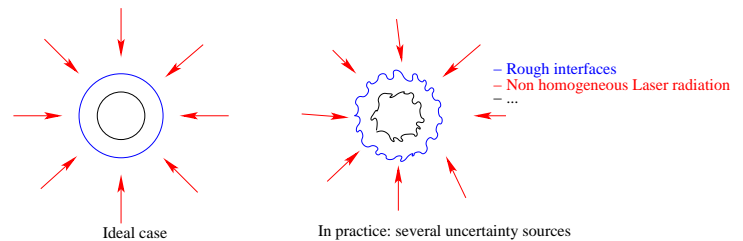

FIGURE 1. Stakes for Inertial Confinment Fusion.

sponds to the ideal case: in practice, the target (interface) is not perfectly smooth and the Rayleigh-Taylor instabilities occuring during the implosion can considerably change the shape of the pellet. If it breaks before the temperature and pressure for ignition are reached, the experience is down. This illustration is representative of the stakes of the problem: experiences are performed and datas are gathered in order to describe the statistics of the perturbations of the interface between the fluids [12]. Given those statistics, we want to propagate uncertainties to the flow.

In this paper, we tackle the problem of propagation of the uncertainties through Euler equations due to initial interface perturbations in stochastic Riemann problems and stochastic **R**ichtmyer-**M**eshkov (RM) like problems [12]. The uncertainty propagation method used is presented in [23, 22] and is based on an Intrusive[1] **g**eneralized **P**olynomial **C**haos (gPC) decomposition [35, 3, 28, 33, 37] adapted to systems of conservation laws

---

[1]The choice of an intrusive method is done according their potential for modelization, see [22] for an illustration.

[25, 26].

In section 1, we present the uncertainty propagation method used to solve the **S**tochastic **P**artial **D**ifferential **E**quations (SPDE) introduced by the latter modelization. Section 2 concerns the discretization of the system resulting from the uncertainty propagation method. The last part, section 3, presents numerical results and physical interpretations.

0.1 Polynomial Chaos (PC) expansion

The resolution of stochastic hyperbolic systems of conservation laws leads to the characterization of stochastic processes. Their approximations, in this paper, are tackled through the application of PC theory [35]: let $(H_k)_{k \in \mathbb{N}}$ denote the normalized one dimensional Hermite polynomials. Let $(\Xi_i)_{i \in \mathbb{N}}$ denote a collection of centered normalized gaussian rv. Then we denote by $(\Psi_{m_1,...,m_d})_{d>0,m_1 \geq 0,...,m_d \geq 0}$ the multidimensional normalized Hermite polynomials obtained by tensorization of the $(H_k)_{k \in \mathbb{N}}$ taken in $(\Xi_i)_{i \in \mathbb{N}}$: we have $\forall d > 0, m_1 \geq 0,...,m_d \geq 0$,

$$\Psi_{m_1,...,m_d}(\Xi_1(\omega),...,\Xi_d(\omega)) = H_{m_1}(\Xi_1(\omega))...H_{m_d}(\Xi_d(\omega)).$$

The ensemble $(\Psi_{m_1,...,m_d})_{d>0,m_1 \geq 0,...,m_d \geq 0}$ forms an orthonormal basis of $L^2(\Omega, \mathscr{F}, \mathscr{P})$, see [3]. The result is the following: let $(F_\beta(\omega))_{\beta \in I, \omega \in \Omega}$ be a stochastic random process,

$$\text{if } \int_{\omega \in \Omega} F_\beta^2(\omega) \mathrm{d}\mathscr{P}(\omega) < \infty, \forall \beta \in I, \text{ then}$$
$$F_\beta(\omega) = \sum_{\substack{P=1 \\ m_1,..,m_P=0}}^{\substack{P=\infty \\ m_1,..,m_P=\infty}} F_{m_1,..,m_P}(\beta) \Psi_{m_1,..,m_P}(\Xi_1(\omega),..,\Xi_P(\omega)),$$

(1)

where[2]

$$F_{m_1,..,m_P}(\beta) = \int_{\omega \in \Omega} F_\beta(\omega) \Psi_{m_1,..,m_P}(\Xi_1(\omega),..,\Xi_P(\omega)) \mathrm{d}\mathscr{P}(\omega).$$

Convergence is in the $L^2(\Omega, \mathscr{F}, \mathscr{P})$-sense and is exponential for gaussian stochastic process. In the case of non gaussian stochastic process, gPC is introduced ([33, 37]), in order to recover spectral convergence[3].

1 Uncertainty Propagation

In the following, we assume that the initial conditions for our uncertain problem have been defined and characterized. We are now interested in the propagation of the uncertainty through Euler equations with *intrusive* gPC methods.

1.1 Intrusive gPC for uncertainty propagation

The classical[4] gPC approach has been extensively applied to uncertainty propagation problems such as stochastic elastic materials [8], finite deformations [2], heat conduction [32], incompressible flows [38, 20, 17], transonic aerodynamics [27, 15, 4], reacting flows and detonation [14], etc. Two variants are important in practice:

the stochastic collocation implementation and spectral projection (non-intrusive) uses a deterministic code as a black-box just as in Monte Carlo based method.
the stochastic Galerkin implementation (intrusive) requires solving a new system.

An intrusive method will be considered in the following: it corresponds to the stochastic equivalent of **F**inite **V**olume (FV) methods in the sense that we do not consider the solution at some discrete points[5] but rather integrals of it against components of the basis.

1.2 Failure of sG-gPC for Systems of Conservation Laws

Despite its application to a large range of domain, the classical[6] intrusive gPC method[7] is not satisfying when applied to systems of conservation laws such as Euler system. The latter system is non linear and might develop discontinuous solutions which precisely corresponds to the weak points of sG-gPC, see [16, 34, 1, 23, 22, 24]. The method is based on a linear Galerkin projection of the system onto the gPC basis. This linear projection can trigger a loss of mathematical[8] and physical[9] properties of the truncated system. Instead, we use a non linear Galerkin projection, IPMM (cf. section 1.3), in order to preserve hyperbolicity of the truncated system.

1.3 Intrusive Polynomial Moment Method (IPMM)

IPMM is adapted to the resolution of non linear stochastic systems of conservation laws, developing shocks and discontinuities such as Euler system. It is based on a non linear Galerkin projection of the system enabling by construction the

---

[2] the coefficients $(F_{m_1,..,m_P}(\beta))_{P>0,m_1 \geq 0,..,m_P \geq 0, \beta \in I}$ are projection of F on the multidimensional basis.

[3] the multidimensional orthornormal basis with respect to the tensorized probability measures of the random variables is used rather than Hermite polynomials: for example, in the case of uniform variables, the associated gPC basis is a tensorization of Legendre polynomials, see [37, 33] for more details.

---

[4] non adaptive, intrusive or non intrusive.

[5] the case of non intrusive methods would correspond to the stochastic equivalent of Finite Differences: it considers punctual values of the solution.

[6] non adaptive.

[7] called **s**tochastic **G**alerkin-**g**eneralized **P**olynomial **C**haos (sG-gPC) in the following.

[8] hyperbolicity, i.e. existence and stability with time of the solutions, see [22, 24].

[9] positiveness or boundedness of certain quantities such as mass density, pressure, etc. [22, 23, 24].

preservation of mathematical and physical properties of the system [22, 23, 24]. Let's apply IPMM to the monodimensional Euler system

$$\begin{cases} \partial_t \rho + \partial_x \rho u = 0, \\ \partial_t \rho u + \partial_x (\rho u^2 + p) = 0, \\ \partial_t \rho e + \partial_x (\rho u e + p u) = 0, \end{cases} \quad (2)$$

where ρ is the mass density, u is the components of the velocity on the x-axis in cartesian coordinates such that $x \in \mathscr{D} \subset \mathbb{R}$, e is the total energy density and p is the pressure of the fluid. The system is closed by an equation of state: in this paper, we consider perfect gas closures for which the pressure has the form $p = (\gamma - 1)\rho \varepsilon$ where $\varepsilon = e - \frac{u^2}{2}$ is the specific internal energy. The system (2) is hyperbolic if $\varepsilon > 0$.

1.3.1 The $P-$truncated Euler system
Let's denote by $U = (\rho, \rho u, \rho e)^t \in \mathscr{U} = \{(\rho, \rho u, \rho e)^t : \varepsilon(\rho, \rho u, \rho e) > 0\}$. Using the equation of state, we introduce the following notations:

$$f(U) = \begin{pmatrix} \rho u \\ \frac{(\rho u)^2}{\rho} + (\gamma - 1)\left(\rho e - \frac{1}{2}\frac{(\rho u)^2}{\rho}\right) \\ \frac{(\rho u)(\rho e)}{\rho} + (\gamma - 1)\frac{\rho u}{\rho}\left(\rho e - \frac{1}{2}\frac{(\rho u)^2}{\rho}\right) \end{pmatrix}.$$

The Euler system (2) can then be rewritten in a more compact form

$$\partial_t U + \partial_x f(U) = 0. \quad (3)$$

Let's suppose initial conditions and boundary conditions are given[10]. We suppose the initial condition is uncertain, modeled by a random vector $\Xi \in \mathbb{R}^Q$ of independent components whose **p**robability **d**ensity **f**unction (pdf) is given by[11] $\mathscr{P}_\Xi$. We denote by $(\phi_k)_{k \in \mathbb{N}}$ the multidimensional gPC basis associated[12] to $\mathscr{P}_\Xi$. Then the $P-$truncated system associated to (3) obtained by a Galerkin projection on the gPC basis is given by

$$\partial_t \begin{pmatrix} U_0 \\ ... \\ U_P \end{pmatrix} + \partial_x \begin{pmatrix} f_0 \\ ... \\ f_P \end{pmatrix} = 0, \quad (4)$$

---

[10]These will be detailed in the numerical results section. We only suppose here that the initial conditions and boundary conditions do not challenge the well-posedness of the system, i.e. the system is hyperbolic for every realizations of the rv modeling the uncertainties, almost surely.

[11]tensorization of the pdfs of the components of the random vector Ξ.

[12]i.e. tensorization of the 1-D polynomials orthonormal with respect to the pdfs of the components of the random vector Ξ (gPC formalism, see [34]).

where $\forall k \in \{0, ..., P\}$:

$$\begin{aligned} U_k &= \int U^P \phi_k \mathrm{d}\mathscr{P}_\Xi, \\ f_k &= \int f(U^P)\phi_k \mathrm{d}\mathscr{P}_\Xi, \text{ with } U^P: \text{ closure to be defined.} \end{aligned} \quad (5)$$

In the case of sG-gPC, the closure of the system is done by considering

$$U \approx U^P = \sum_{k=0}^P U_k \phi_k \text{ (sG-gPC)}, \quad (6)$$

corresponding to a linear projection of the solution U on the gPC basis. This closure fails to preserve the important properties of the system mainly because of the apparition of discontinuous solutions triggering Gibbs phenomenon, see [23, 22, 24]. In the following section, we present a closure consistent with the preservation of hyperbolicity of the $P-$truncated system. The closure is based on the application of moment theory [10, 18, 19] to system (4).

1.3.2 A consistent closure for Euler System
Applying Moment theory to close the system consists in solving the underdetermined inverse problem:

$$\begin{aligned} &\text{Find } U^P \in L^2(\Omega, \mathscr{F}, \mathscr{P}) / \\ &\begin{cases} \int U^P \phi_0 \mathrm{d}\mathscr{P} = U_0, \\ ..., \\ \int U^P \phi_k \mathrm{d}\mathscr{P} = U_k, \\ ..., \\ \int U^P \phi_P \mathrm{d}\mathscr{P} = U_P, \end{cases} \quad (7) \end{aligned}$$

where $(\phi_i)_{i \in \{0,...,P\}}$ is the gPC basis of $L^2(\Omega, \mathscr{F}, \mathscr{P})$. The distribution U^P, solution of (7) is not unique: in Moment theory, one introduces the closure (Shannon) entropy

$$\eta(f) = \int f \ln(f) \mathrm{d}\mathscr{P}. \quad (8)$$

This results in a well posed moments problem: find U^P as the minimum of η under the constraints (7).

Let's apply Moment theory to our system. Let θ be a strictly convex functional of U. This function θ, *the closure entropy*, is the main degree of freedom of IPMM. We close the system (4) by finding the Lagrange multipliers $(\lambda_k)_{k \in \{0,...,P\}}$ minimizing the

functional[13]

$$T(\lambda_0,..,\lambda_P) = -\int \theta(U^P(\lambda_0,..,\lambda_P))\mathrm{d}\mathscr{P}$$
$$+\sum_{k=0}^{P}\int U^P(\lambda_0,..,\lambda_P)\lambda_k\phi_k\mathrm{d}\mathscr{P} - \sum_{k=0}^{P}U_k\lambda_k. \tag{9}$$

By performing some functional variations in T with respect to U^P, we obtain U^P with the particular form[14]:

$$\nabla_U \theta(U^P(\lambda_0,..,\lambda_P)) = \sum_{k=0}^{P}\lambda_k\phi_k \qquad \text{or also}$$
$$U^P(\lambda_0,..,\lambda_P) = (\nabla_U\theta)^{-1}\left(\sum_{k=0}^{P}\lambda_k\phi_k\right) \text{ (IPMM).} \tag{10}$$

Consequently, in the gPC formalism, IPMM consists in developing the new variable $\nabla_U\theta(U^P(\lambda_0,...,\lambda_P))$, called *associate variable*, on the gPC basis rather than the main variable U. This enables to close the system (4).

Let's now work with different entropies:

If we choose $\theta(U) = \frac{U^2}{2}$, then $U^P = (\nabla_U\theta)^{-1}(\lambda) = U$: in this case, the associate variable is the main variable U and IPMM degenerates into sG-gPC.

Now consider the special case $\theta = s$ where s denote the mathematical entropy[15] of (3): the closure entropy is chosen as the mathematical entropy of the studied system of conservation laws, here Euler system. Then $\nabla_U s(U) = \lambda = V$, called the *entropic variable* in the formalism of [19].

The latter case is particularly interesting: the entropic variable has the property of symmetrizing the system of conservation laws ensuring its hyperbolicity [25]. By developing this entropic variable V on the gPC basis rather than the main variable U, we ensure the construction of a hyperbolic $P-$truncated system. The preservation of the physical properties is a corollary of hyperbolicity, see [23, 24, 22].

Euler system has a strictly convex mathematical entropy[16] given by (s, g) where

$$s(\rho, \rho u, \rho e) = -\rho\ln\left(\rho^{-\gamma}\left(\rho e - \frac{(\rho u)^2}{2\rho}\right)\right) \tag{11}$$

with its entropy flux

$$g(\rho, \rho u, \rho e) = \frac{\rho u}{\rho}s(\rho, \rho u, \rho e). \tag{12}$$

Note that this mathematical entropy is the opposite of the physical entropy of Euler system.

We will use this mathematical entropy as a closure entropy in the following so that hyperbolicity of the $P-$truncated Euler system is ensured.

The entropic variable $V = (v_1, v_2, v_4)^t$ associated to s is given by

$$V(U) = \begin{pmatrix} -\ln\left(\frac{2(\rho e)\rho - (\rho u)^2 - (\rho v)^2}{2\rho^{\gamma+1}}\right) \\ +\gamma - \frac{(\rho u)^2 + (\rho v)^2}{2\rho(\rho e) - (\rho u)^2 - (\rho v)^2} \\ \frac{2\rho(\rho u)}{2\rho(\rho e) - (\rho u)^2 - (\rho v)^2} \\ -\frac{2\rho^2}{2\rho(\rho e) - (\rho u)^2 - (\rho v)^2} \end{pmatrix}, \tag{13}$$

and the bijection $V :\longrightarrow U(V)$ is given by

$$U(V) = \begin{pmatrix} \exp\frac{2v_1 v_4 - 2v_4\ln(-v_4) - 2v_4\gamma - v_2^2}{2v_4(\gamma-1)} \\ -\frac{v_2}{v_4}\exp\frac{2v_1 v_4 - 2v_4\ln(-v_4) - 2v_4\gamma - v_2^2}{2v_4(\gamma-1)} \\ \frac{v_2^2 - 2v_4}{2v_4^2}\exp\frac{2v_1 v_4 - 2v_4\ln(-v_4) - 2v_4\gamma - v_2^2}{2v_4(\gamma-1)} \end{pmatrix}. \tag{14}$$

Note that the first component of V in (14) corresponds to the mass density ρ: its positiveness is ensured by construction due to the exponential form of $\rho(V)$. This still holds when V is developed on a gPC basis.

Let's develop V on the polynomial basis: we note

$$\forall k \in \{0,...,P\}, V_k = \int V\phi_k\mathrm{d}\mathscr{P}_\Xi. \tag{15}$$

The full system we solve is given by

$$\partial_t\begin{pmatrix} U_0(V_0,..,V_P) \\ ... \\ U_P(V_0,..,V_P) \end{pmatrix} + \partial_x\begin{pmatrix} f_0(V_0,..,V_P) \\ ... \\ f_P(V_0,..,V_P) \end{pmatrix} = 0, \tag{16}$$

where $U_0,...,U_P$, $f_0,...,f_P$ and $h_0,...,h_P$ are given by (5) with[17] $U^P(V_0,...,V_P) = U(\sum_{k=0}^{P}V_k\phi_k)$. Finally, $V_0,...,V_P$ is the vector of

---

[13] minimization of θ under the constraints (7).

[14] The inversion of $\nabla_u\theta$ is possible as, by hypothesis, θ is strictly convex.

[15] By definition of the mathematical entropy, s is strictly convex, see [25].

[16] Actually, it exists several strictly convex mathematical entropies for Euler system, see [25, 23], but we will only consider the following in this paper.

[17] where $V \longrightarrow U(V)$ is defined by (14).

Lagrange multipliers minimizing the functional:

$$
\begin{aligned}
T(V_0,..,V_P) = & -\int s(U^P(V_0,..,V_P))\mathrm{d}\mathscr{P} \\
& + \sum_{k=0}^{P}\int U^P(V_0,..,V_P)V_k\phi_k\mathrm{d}\mathscr{P} - \sum_{k=0}^{P} U_k V_k,
\end{aligned}
\tag{17}
$$

where s is defined by (11). This system is hyperbolic.

2 Discretization of the $P-$truncated System of Conservation Laws (16)–(17)

In this section, we detail the discretization of system (16)–(17). The first section concerns the numerical scheme used to discretize (16). This step is common with the sG-gPC approach. The second one deals with the discretization of closure (17). This latter is composed of two main steps: the evaluation of the integral in (17) and the minimization algorithm.

2.1 Discretization of (16): FV scheme

The discretization of (16) is done thanks to a High-order 1-D Lagrange + Remap FV scheme with directional splitting. The different steps are developed in the next sections. For more details about FV schemes, we refer to [6].

2.1.1 1-D FV scheme
We first describe 1-D FV schemes. The extension in 2-D is done by directional splitting, see [22]. In this section, we want to discretize the first part of the splitted system (16)[18]

$$
\partial_t \begin{pmatrix} U_0 \\ ... \\ U_P \end{pmatrix} + \partial_x \begin{pmatrix} f_0 \\ ... \\ f_P \end{pmatrix} = 0.
\tag{18}
$$

We define the control volume $]t^n,t^{n+1}[\times]x_{i-\frac{1}{2}},x_{i+\frac{1}{2}}[$, we note $\Delta t = t^{n+1} - t^n$ and $\Delta x_i = x_{i+\frac{1}{2}} - x_{i-\frac{1}{2}}$. In the following, we suppose the 1-D physical space $x \in \mathscr{D}_x$ is discretized in N_x finite volumes. We define

$$
U_{k,i}^n = \frac{1}{\Delta x_i}\int_{x_{i-\frac{1}{2}}}^{x_{i+\frac{1}{2}}} U_k(x,t^n)\mathrm{d}x,
\tag{19}
$$

$$
\forall k \in \{0,...,P\}, \forall i \in \{1,...,N_x\},
\tag{20}
$$

and

$$
f_{k,i+\frac{1}{2}}^* = \frac{1}{\Delta t}\int_{t^n}^{t^{n+1}} f_k(x_{i+\frac{1}{2}},t)\mathrm{d}t,
\tag{21}
$$

$$
\forall k \in \{0,...,P\}, \forall i \in \{1,...,N_x\},
\tag{22}
$$

---

[18]here, we drop the dependences with respect to V.

such that on the control volume $]t^n,t^{n+1}[\times]x_{i-\frac{1}{2}},x_{i+\frac{1}{2}}[$, (18) is equivalent to

$$
\frac{1}{\Delta t}\begin{pmatrix} U_{0,j}^{n+1} - U_{0,j}^n \\ ... \\ U_{P,j}^{n+1} - U_{P,j}^n \end{pmatrix} + \frac{1}{\Delta x_j}\begin{pmatrix} f_{0,j+1/2}^* - f_{0,j-1/2}^* \\ ... \\ f_{P,j+1/2}^* - f_{P,j-1/2}^* \end{pmatrix} = 0,
\tag{23}
$$

Sofar, no approximation has been taken: i.e. the discretization of (23) begins with the definition of the numerical fluxes $(f_{k,i+\frac{1}{2}}^*)_{k\in\{0,...,P\},i\in\{1,...,N_x\}}$ and $(f_{k,i-\frac{1}{2}}^*)_{k\in\{0,...,P\},i\in\{1,...,N_x\}}$.

The FV formulation is adapted to the kind of equation considered: conservativity of $(U_k)_{k\in\{0,...,P\}}$ on the domain $\mathscr{D}_x$ is ensured by construction and the definition of $f_{k,i+\frac{1}{2}}^*$ is consistent with the non linearity of the flux of system (18). The approach considers means of the solution U on control volumes rather than discrete values of it, which could not be defined due to the presence of discontinuities.

The full system (16) is solved thanks to directional splitting, see [22]. It remains to describe the numerical scheme used in the 1-D phases of the directional splitting. Replacing the expressions (5) in (21) gives

$$
f_{k,j+\frac{1}{2}}^* = \frac{1}{\Delta t}\int_{t^n}^{t^{n+1}}\int f\left(U\left(\sum_{i=0}^{P} V_i(x_{j+\frac{1}{2}},t)\phi_i\right)\right)\phi_k\mathrm{d}\mathscr{P}_\Xi\mathrm{d}t.
\tag{24}
$$

There exists several ways to discretize the flux $f_{k,i+\frac{1}{2}}^*$ (Roe scheme [22]...). In this paper, we use the Lagrange+Remap scheme: its application relies on the fact that the FV formulation commutes with the stochastic integrals with respect to $\mathscr{P}_\Xi$. Then, we have

$$
\begin{aligned}
f_{k,j+\frac{1}{2}}^* &= \int \frac{1}{\Delta t}\int_{t^n}^{t^{n+1}} f\left(U\left(\sum_{i=0}^{P} V_i(x_{j+\frac{1}{2}},t)\phi_i\right)\right)\mathrm{d}t\,\phi_k\mathrm{d}\mathscr{P}_\Xi, \\
f_{k,j+1/2}^* &= \int f_{j+1/2}^*(\Xi)\phi_k(\Xi)\mathrm{d}\mathscr{P}_\Xi.
\end{aligned}
$$

The discretized system becomes

$$
\begin{pmatrix} \frac{U_{0,j}^{n+1}-U_{0,j}^n}{\Delta t} \\ ... \\ \frac{U_{P,j}^{n+1}-U_{P,j}^n}{\Delta t} \end{pmatrix} + \begin{pmatrix} \frac{\int f_{j+\frac{1}{2}}^*\phi_0\mathrm{d}\mathscr{P}_\Xi - \int f_{j-\frac{1}{2}}^*\phi_0\mathrm{d}\mathscr{P}_\Xi}{\Delta x_j} \\ ... \\ \frac{\int f_{j+\frac{1}{2}}^*\phi_P\mathrm{d}\mathscr{P}_\Xi - \int f_{j-\frac{1}{2}}^*\phi_P\mathrm{d}\mathscr{P}_\Xi}{\Delta x_j} \end{pmatrix} = 0.
\tag{25}
$$

The integrals in the flux are evaluated by standard numerical quadratures described in section 2.2. This procedure enables to have the choice of the numerical scheme: in our case, $\left(f_{j+1/2}^*(\xi_l)\right)_{l\in\{1,...,N_q\}}$, the components of the flux evaluated at the quadrature points are calculated using the Lagrange+Remap scheme of arbitrary high-order based on the acoustic Godunov solver. More details are given in [9, 22].

2.2 Discretization of the closure (17): robustness condition

The discretization of the minimization algorithm requires two steps: it first needs the use of numerical integration technics to evaluate the hessian of the functional T. The second step concerns the minimization algorithm used to close the system.

The discretization step enabling to obtain the moments of the solution at time step $n+1$ from moments of the solution at time step n has been described in section 2.1. We here tackle the step enabling to obtain the moments of the entropic variable $(v_{k,i}^{n+1})_{k\in\{0,...,P\},i\in\{1,...,N_x\}}$ from the moments of the main variable $(u_{k,i}^{n+1})_{k\in\{0,...,P\},i\in\{1,...,N_x\}}$: it consists in the minimization of the following functional

$$
\begin{aligned}
T(v_{0,i}^{n+1},...,v_{P,i}^{n+1}) = &\int s^*\left(\sum_{k=0}^{P} v_{k,i}^{n+1}\right) d\mathscr{P}_\Xi \\
&- \sum_{k=0}^{P}\left\langle u_{k,i}^{n+1}, v_{k,i}^{n+1}\right\rangle,
\end{aligned}
\tag{26}
$$

in every cells $i\in\{1,...,N_x\}$. In (26), the Legendre transform s^* of the entropy s has been introduced. The first step for the determination of $(v_{k,i}^{n+1})_{i\in\{1,...,N_x\}}$ consists in discretizing the integral in (26).

We first describe 1-D quadrature rules, then we will develop on the multidimensional ones. For more details, we refer to [11] and the references therein.

2.2.1 Discretization of functional T
The last step of IPMM consists in the minimization of the discretized version of (26)

$$
\begin{aligned}
&T(v_{0,i}^n,...,v_{P,i}^n) \approx \\
&\widetilde{T}(v_{0,i}^n,...,v_{P,i}^n) = \sum_{l=1}^{N_q} s^*\left(\sum_{k=0}^{P} v_{k,i}^n \phi_k(\xi_l)\right) w_l \\
&\qquad\qquad - \sum_{k=0}^{P}\left\langle u_{k,i}^n, v_{k,i}^n\right\rangle,
\end{aligned}
\tag{27}
$$

where $(\xi_l)_{l\in\{1,...,N_q\}}$ are the N_q points of the chosen quadrature and $(w_l)_{l\in\{1,...,N_q\}}$ the associated weights. For simplicity, we drop the cell and time indices: the hessian of $\widetilde{T}$ is given by

$$
\tag{28}
$$

$$
\nabla_{V,V}^2\widetilde{T}(v_0,...,v_P) = \sum_{l=1}^{N_q} w_l \nabla_{v,v}^2 s^*\left(\sum_{k=0}^{P} v_k\phi_k(\xi_l)\right)\cdot\Phi(\xi_l).
$$

where

$$
\Phi(\xi_l) = \begin{pmatrix} \phi_0(\xi_l)\phi_0(\xi_l) & ... & \phi_0(\xi_l)\phi_P(\xi_l) \\ ... & \phi_i(\xi_l)\phi_j(\xi_l) & ... \\ \phi_P(\xi_l)\phi_0(\xi_l) & ... & \phi_P(\xi_l)\phi_P(\xi_l) \end{pmatrix}.
\tag{29}
$$

The discretized functional $\widetilde{T}$ (27) has a minimum if matrix (28) is definite positive. Let $X = (x_0,...,x_P)^t \in \mathbb{R}^{n\times(P+1)}$ be non zero, then, denoting by[19] $\Pi^P m(\xi_l) = \sum_{k=0}^{P} m_k\phi_k(\xi_l)$, we obtain:

$$
\begin{aligned}
&\left\langle X, \nabla_{V,V}^2\widetilde{T}(v_0,...,v_P)X\right\rangle_{n\times(P+1)} = \\
&\sum_{l=1}^{N_q}\left\langle \Pi^P x(\xi_l), \nabla_{v,v}^2 s^*\left(\Pi^P v(\xi_l)\right)\Pi^P x(\xi_l)\right\rangle_n w_l, \\
&\geq \min_{\substack{l\in\{1,...,N_q\} \\ k\in\{0,...,P\}}} \lambda_k\left(\Pi^P v(\xi_l)\right) \times \sum_{l=1}^{N_q}\left(\Pi^P x(\xi_l)\right)^2 w_l.
\end{aligned}
$$

The hessian matrix of s^* being, by definition[20], definite positive, we have

$$
\min_{\substack{l\in\{1,...,N_q\} \\ k\in\{0,...,P\}}} \lambda_k\left(\sum_{i=0}^{P} v_i\phi_i(\xi_l)\right) > 0.
$$

Consequently, the hessian matrix of $\widetilde{T}$ is definite positive under the condition

$$
\sum_{l=1}^{N_q}\left(\sum_{i=0}^{P} x_i\phi_i(\xi_l)\right)^2 w_l > 0.
\tag{30}
$$

This condition is satisfied in the case of fully tensorized quadrature rule (indeed, all weights $(w_l)_{l\in\{0,...,n_q\}}$ are positive). In the case of an isotropic sparse quadrature, those weights can be negative and trigger difficulties: it is nevertheless possible to show

---

[19] for $m\in\{x,v\}$.
[20] Legendre transform of a strictly convex function.

that if (sufficient condition)

$$\sum_{l=1}^{N_q} \phi_k(\xi_l)\phi_t(\xi_l)w_l = \delta_{k,t}, \forall (k,t) \in \{0,...,P\}^2, \qquad (31)$$

then the discretized functional (27) is strictly convex and has a unique minimum.

For a given truncature order P, it is possible to deduce *a priori* the level of the quadrature rule needed to satisfy the robustness of the algorithm: the quadrature rule must integrate exactly polynomials of degree $2P$. For a Gauss quadrature for example, P points would be enough.

2.2.2 Minimization algorithm for $\widetilde{T}$

Let's suppose conditions (30) – (31) are satisfied:

The functional $\widetilde{T}$ is consequently strictly convex, its minimum is unique.

The mathematical entropy[21] is given: the expression of $\nabla_{v,v}^2 s^*$ is known analytically.

According to these hypothesis, we use a Newton algorithm to minimize $\widetilde{T}$. The guess is given by the vector of moments of v at the precedent time step. The conditions are satisfied to ensure quadratic convergence of the Newton algorithm. The different steps are described in table 1. The inversion of the hessian

Minimization of the str. convex $\widetilde{T}(V) = S^*(V) - \left\langle U_i^{n+1}, V \right\rangle$.

Newton
$$\begin{cases} \text{-} \ V^k \rightarrow V^{k+1}, \\ \text{-} \ V^{k+1} = V^k - \left(\nabla_{V,V}^2 \widetilde{T}(V^k)\right)^{-1} \nabla_V \widetilde{T}(V^k), \\ \text{-} \ ||V^{k+1} - V^k|| < \varepsilon_{Newt} = 10^{-13}, \\ \text{-} \ \text{with } V_i^n \text{ as guess.} \end{cases}$$

TABLE 1. Newton algorithm.

matrix of T is exact (LU decomposition). The same choice is done in [18]. The algorithm converges in 5 to 6 iterations for a threshold of 10^{-13} and about 9 polynomial moments (similar results as in [18]).

For computation needing a higher number of polynomial moments (high stochastic dimensions and/or high polynomial order) a conjugate gradient method is used. It enables to avoid the matrix inversion of size $n \times (P+1)$, costful when P grows.

3 Numerical Results

In this section, we first describe two one dimensional test cases (Sod and Richtmyer-Meshkov like, see subsections 3.0.3 and 3.0.4): these simplified problems enable to understand more easily the dynamics of the more complex flows tackled afterward: for example, we give details on the velocity and pressure for these test cases only and we focus on the mass density and the interface between the fluids in the 2-D simulations[22].

In the next subsections, we first describe the statistics of the perturbed interface position before propagating the uncertainty through the Euler system with IPMM. Numerical results are presented with physical interpretations.

3.0.3 Stochastic Riemann Problem: uncertain Sod shock tube

Let's first consider a stochastic Riemann problem. The uncertainty is carried on the interface position separating a light and a heavy fluid. The adiabatic coefficient of the perfect gas closure is $\gamma = 1.4$ and the initial condition is given by

$$\begin{cases} \rho(x,0,\Xi) &= \begin{cases} 1 \text{ if } x \leq x_{interface}(\Xi), \\ 0.125 \text{ else,} \end{cases} \\ \rho u(x,0,\Xi) = 0, \\ \rho e(x,0,\Xi) &= \begin{cases} 2.5 \text{ if } x \leq x_{interface}(\Xi), \\ 0.25 \text{ else.} \end{cases} \end{cases} \qquad (32)$$

The interface position is modelized by uniform random variable on $[-1,1]$:

$$x_{interface}(\Xi) = 0.5 + 0.05\Xi.$$

Remark 3.0.1. *We recall that in practice, the code is intrusive and is consequently initialized by computing the moments of the main variable. The latter description of the initialization is more compact.*

For one realization of the random variable, we recall that the solution consists in one shock, propagating in the *light* fluid (right of the interface), one contact discontinuity and one rarefaction fan in the *heavy* fluid.

Remark 3.0.2. *Note that the sG-gPC method do not enable to solve this problem: oscillations due to Gibbs phenomenon in the uncertain domain foster negative mass densities ($\Pi^P \rho$) in certain areas of the uncertain domain: this leads to a crash of the numerical scheme.*

---

[21]which is also the closure entropy.

[22]Indeed, u and p are continuous through the interface and do not give more information.

For early times of the simulations, the uncertainty is mainly localized at the center of the domain. As time passes, three distinct regions are appearing. The variance is zero and the mean is constant between these regions. The uncertainty on the contact discontinuity and the shock advected. The distribution are symetric and have the same amplitudes. The velocities of the waves are not affected by the uncertain parameter for this test-case. The behaviour of the statistic of the rarefaction fan is more complex. The uncertainty seems to propagate in the left part of the curve assymetrically: this change in the form of the distribution is a consequence of the non linearity of the problem. Figure 2 shows also the mean and variance of the velocity and the pressure of the fluid at $t = 0$ and $t = 0.14$. The same remarks can be made about the velocity and the pressure: the uncertainty is propagated between the shock wave and the rarefaction fan. Note that initially, the uncertainty on the fluid velocity is zero on the whole domain and becomes more and more important as time passes, especially in the shock vicinity. The asymetry in the variance of the rarefaction fan for the mass density is also visible on the variance of the rarefaction fan in the pressure distribution. On the contrary, the rarefaction fan for the velocity remains perfectly symetric as time passes.
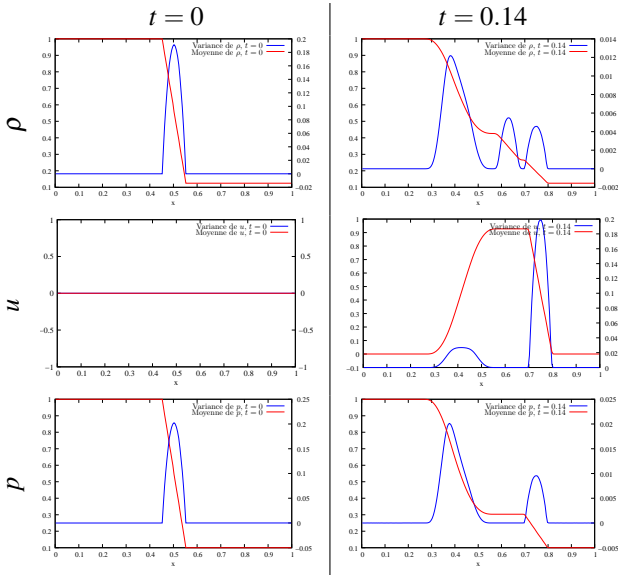
it has $n \times (P+1) = 3 \times (P+1)$ finite waves. The four figures represent the mean and variance of the mass density ρ at $t = 0.14$ for test-case (32), for two different polynomial orders $P = 4$ and $P = 20$ and for two spatial discretizations, 200 and 500 cells. As we refine in the physical space, some structures appear in the vicinity of the shock wave. According to the truncation order, these structures will be different: for a given P, there will be $P+1$ waves in the vicinity of the mean of the shock (also identifiable in the vicinity of the shock for the variance of the mass density, velocity, pressure). The non truncated system has three distinct eigenvalues $u-c, u, u+c$ corresponding to the different waves (shock, interface, rarefaction). Figure 3 leads to think that the truncated system has $P+1$ rarefaction waves and $P+1$ shock waves[23] and wonder about the last wave[24]: the theoretical verification of this postulat is hard to carry out and is beyond the scope of the paper[25]. Note also that the same kind of phenomenon can appear by applying non intrusive methods, it is briefly described in the annexes of [22].
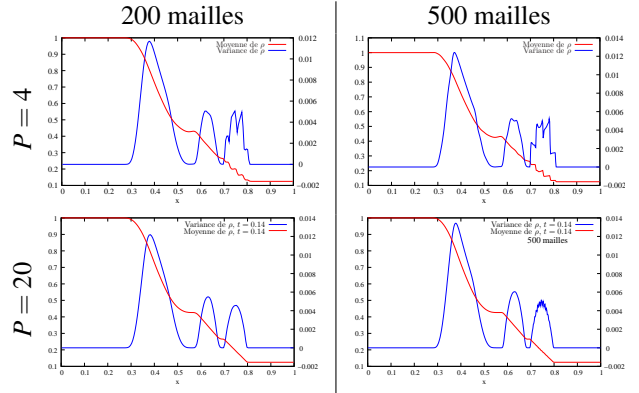

FIGURE 3. Stochastic Riemann problem with initial conditions (32). The computations has been made with 200 and 500 cells for $P = 4$ and $P = 20$. Level 7 in the 1-D Clenshaw-Curtis rule is used for numerical integration. The hyperbolic structure of the truncated system appears, especially in the vicinity of the uncertain shock: $P+1$ waves. This constatation is indepedent of the intrusive spectral uncertainty propagation method used, these waves are inherent to the considered truncated system.

FIGURE 2. Stochastic Riemann Problem whose initial conditions are given by (32). The left column shows the initial conditions for the mean and std of ρ, u, p. The right column shows the mean and std of ρ, u, p at final time $t = 0.14$. The calculation has 200 cells, $P = 20$. A level 7 in the 1-D Clenshaw-Curtis rule is used for numerical integration. We used a third order Lagrange+Remap scheme ([9]).

Figure 3 emphasizes the structure of the truncated system: indeed, the truncated system (16) being hyperbolic, we know that

3.0.4 Richtmyer-Meshkov-like test-case (1-D adaptated)
Richtmyer-Meshkov (RM) test case is a two

---

[23]$2 \times (P+1)$ eigenvalues really nn linear cf. [25].

[24]which, on the contrary is only linearly degenerated, see [25].

[25]Indeed, in order to verify this hypothesis, computations on the eigenvalues and eigenvectors are necessary. For the truncated Euler system (16) we consider, the explicit analytical expressions of these are very difficult to obtain $for all P \in \mathcal{N}$ and constitutes a very difficult problem. Note that this observation, to our knowledge, has not been tackled in Moment theory papers/books.

dimensional problem in which a shock propagating in a fluid hits an non moving interface between a light and a heavy fluid. When this interface is perturbed, hydrodynamical instabilities are developping. The 1-D test case solved in this section is inspired of the RM one. In 1-D spatial coordinates, the perturbed interface is modeled by a random variable translating the interface on the x-axe. The initial conditions are given by

$$
\begin{cases}
\rho(x,0,\Xi) = \begin{cases} 4, & \text{if } x \leq x_{interface}(\Xi). \\ 1, & \text{if } x_{interface}(\Xi) \leq x \leq x_{shock}. \\ \dfrac{2\gamma - \gamma s + s}{2\gamma - \gamma s - s}, & \text{if } x \geq x_{shock}. \end{cases} \\[2mm]
u(x,0,\Xi) = \begin{cases} 0, & \text{if } x \leq x_{interface}(\Xi). \\ 0, & \text{if } x_{interface}(\Xi) \leq x \leq x_{shock}. \\ -\sqrt{\dfrac{s(\rho - 1)}{\rho(1-s)}}, & \text{if } x \geq x_{shock}. \end{cases} \\[2mm]
p(x,0,\Xi) = \begin{cases} 1, & \text{if } x \leq x_{interface}(\Xi). \\ 1, & \text{if } x_{interface}(\Xi) \leq x \leq x_{shock}. \\ \dfrac{1}{1-s}, & \text{if } x \geq x_{shock}. \end{cases}
\end{cases}
\tag{33}
$$

On the left hand side to the inteface, a heavy fluid is at rest. On the right hand side, a shock is initialized at $x_{shock} = 0.7$ in the light fluid. For $t > 0$ the shock propagates toward the interface. The coefficient s in (33) denotes the strength of the shock. In practice, we take $s = 0.5$ and $\gamma = 1.4$. The uncertainty on the interface is modeled by random variable: $x_{interface} = 0.5 + 0.05\Xi$ where Ξ is an uniform random variable on $[-1,1]$[26].

For one realization of the random variable, the test case presents two steps: the first one consists in the arrival of the shock on the interface. The second one consists in the interaction of the shock with the interface giving birth to two shock waves propagating in both directions. The first wave is the transmitted shock, in the heavy fluid, and the second is the reflected shock, in the light fluid.

Figure 4 shows the mean and std of the mass density, velocity and pressure at times $t = 0$ and $t = 0.34$. Initially, only the mass density is uncertain as on each side of the interface, pressure and velocity are equals (cf. the ordinate axe on the right of figure 4, the std at $t = 0$ of the velocity and pressure are zero).

When the shock hits the uncertain interface, two waves appears and propagates in the light and heavy fluid: the uncertainty is shared between the three waves corresponding to the mean/std of the transmitted shock, the interface and the reflected shock The uncertainty area in the vicinity of the interface is compressed as the std of the mass density is more than doubled.

---

[26]W have given the initial conditions for the mass density, velocity and pressure for this test case: in practice, the initialization is done with the polynomial moments of the conservative variables, $\rho_0, ..., \rho_P, (\rho u)_0, ..., (\rho u)_P, (\rho e)_0, ..., (\rho e)_P$, but is not convenient for representation.

Remark 3.0.3. *We have tested the sG-gPC method on this test case: when the shock hits the interface, the sG-gPC code crashes due to the appearance of Gibbs phenomenon. Indeed, the amplitude of the contact discontinuity at this time is more than doubled, and realizations of the mass density with sG-gPC are negative and the difficulties described in the precedent subsection (or also in [23]) are encountered: note that in this test case, those numerical difficulties appear dynamically during the computation and not at the initialization.*

After the interaction shock-interface, the uncertainty is propagated at the velocity and pressure of the fluid, in the vicinities of the transmitted and reflected shocks. Further these areas, for this test case, the std is zero.
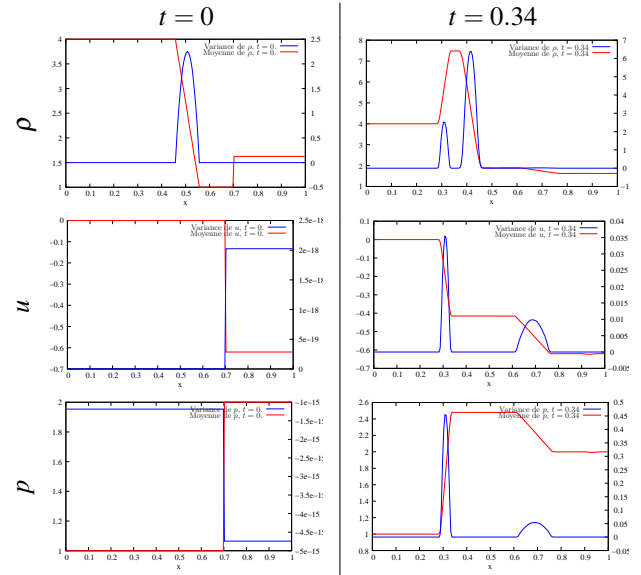

FIGURE 4. 1-D Richtmyer-Meshkov like problem whose initial conditions are given by (33). The left column shows the initial conditions for the mean and std of ρ, u, p. The right column shows the mean and std of ρ, u, p at final time $t = 0.34$. The computation has 200 cells, $P = 20$. A level 7 in the 1-D Clenshaw-Curtis rule is used for numerical integration.

3.0.5 2-D Stochastic Riemann problem, axisymmetric geometry

The uncertainty is carried by the interface position between the light and heavy fluid. In the following subsections, we denote $r = \sqrt{x^2 + y^2}$. The adiabatic coefficient of the considered perfect gas is $\gamma = 1.4$ and the initial conditions are

given by

$$
\begin{cases}
\rho(x,y,0,\Xi) &= \begin{cases} 1 \text{ if } r \leq r_{interface}(\Xi) \\ 0.125 \text{ elsewhere,} \end{cases} \\
\rho u(x,y,0,\Xi) = 0, \\
\rho v(x,y,0,\Xi) = 0, \\
\rho e(x,y,0,\Xi) &= \begin{cases} 2.5 \text{ if } r \leq r_{interface}(\Xi) \\ 0.25 \text{ elsewhere.} \end{cases}
\end{cases}
\tag{34}
$$

These initial conditions are also recalled figure 5 (left). The boundary conditions are of wall type on the left and bottom boundaries of the simulation domain and of neutral type on the two others.

The uncertain interface position is modeled by a uniform random variable on $[-1,1]$, on the sur radius $r_{interface}(\Xi) = 0.7 + 0.1\Xi$. The std of $r_{interface}(\Xi)$ is doubled in comparison with the 1-D problem (32).

For one realization of the random variable, we recall that the solution consists in a shock propagating in the light fluid (right of the interface) and a rarfaction fan in the heavy fluid (left of the inteface) separated by a contact discontinuity (interface).
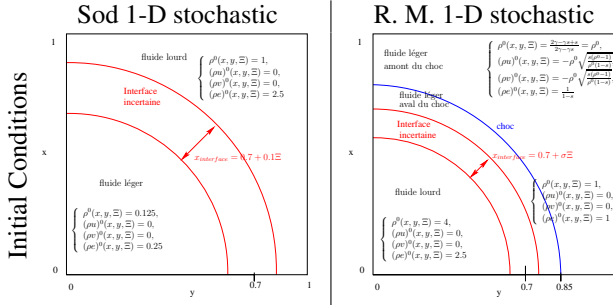

FIGURE 5. Initial conditions for the stochastic Riemann problem, given also by (34) and for the stochastic, also given by (35).

Figure 6 shows the initial conditions and the solution at final time $t = 0.24$ for the mean and std of the mass density . Three distinct waves are propagating their support is in fact in relationship with the variability areas of the three waves of the deterministic system (shock, interface, rarefaction fan): the uncertainty is more important in their vicinities.

Figure 7 shows the pdfs of the mass density at four points of the physical domain, located in the variability domains of the shock, the contact discontinuity, the floor between the interface and the rarefaction and the rarefaction. For the two first positions (figure 7 top), the pdfs present two distinct modes corresponding to the highest probabilities for the realizations of the random variable $\rho(x,t,\Xi)$: these modes correspond to the floors of the shock (left) and of the interface (right). Note that the axisymmetric 2-D Sof test case is different from the 1-D one as

the floors of the shock and interface are not constant: this is in agreement with the fact that, for example on figure 7 left, the mode near $\rho = 0.34$ is spread on the interval $[0.3, 0.4]$. The same remark can be made for figure 7 right: the spreading of the modes on the histograms are physical. The pdfs shows that the random variable "mass density" tends toward a discrete random variable in the vicinity of the discontinuities. Figure 7 bottom shows the pdfs of the mass density at two other locations in the simulation domain in which the solution is continuous: at these locations, the random variable "mass density" is a continuous random variable.

Remark 3.0.4. *Note that in the context of gPC [33], the latter study tends to show that the chosen PC basis can not be optimal in every cells and every times of the simulation: [31, 7] work on time adaptive gPC method based on the search of the optimal decomposition with time and space location.*
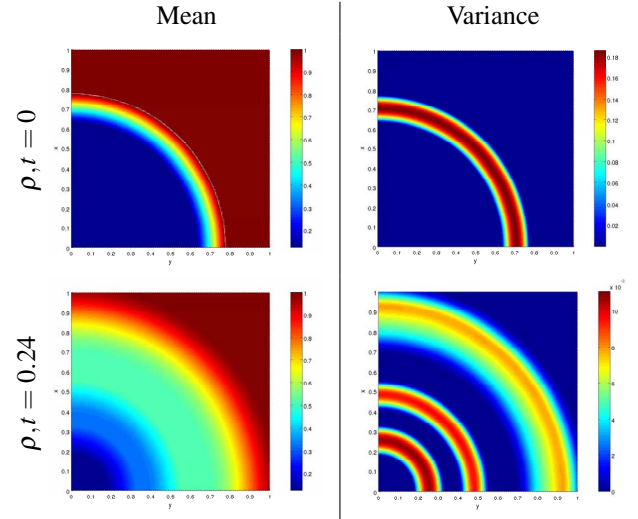

FIGURE 6. Stochastic Riemann problem with initial conditions given by (34). The left column shows the means of the mass density at times $t = 0$ and $t = 0.24$, the right column shows the std of ρ at times $t = 0$ and $t = 0.24$. The computation has 200×200 cells, $P = 20$. A level 7 in the 1-D Clenshaw-Curtis rule is used for numerical integration.

Figure 8 shows several moments of the mass density $(\rho_1, \rho_2, \rho_3, \rho_4, \rho_{10}$ and $\rho_{20})$ with respect to x and y at time $t = 0.24$. The results are extracted from the same simulation as those of figure 6. This figure shows how the increase in the polynomial order affects the resolved statistic of the flow. For example, low orders ensure a good resolution of the statistic of the rarefaction fan (this is directly link with the smoothness of the deterministic wave): the 10th moment do not contribute anymore for the accuracy of the rarefaction fan (cf. figure 8 bottom left). The
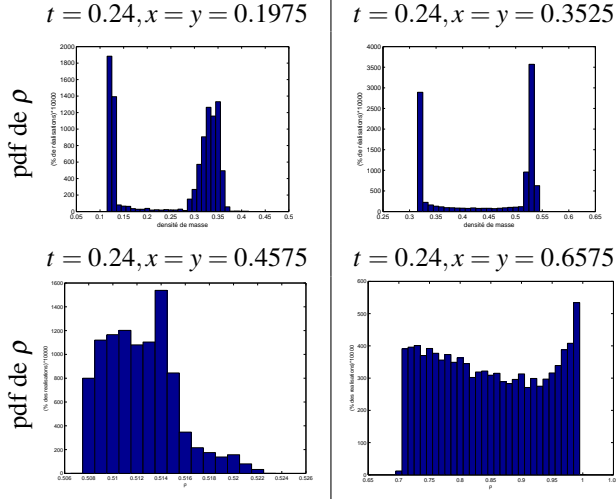
FIGURE 7. Stochastic Riemann problem with initial conditions given by (34). The figure shows the pdfs of the mass density at four spatial locations $x = y = 0.1975$ (top left), $x = y = 0.3525$ (top right), $x = y = 0.4575$ (bottom left) and $x = y = 0.6575$ (bottom right) at time $t = 0.24$. The pdfs are obtained from the numerical simulation of figure 6. For the two first positions (top pictures), two modes are identifiable corresponding to the floors of the shock (left) and of the interface (right).

modes in the vicinity of the shock and interface are still represented for this moment ρ_{10}. At order 20, see figure 8 bottom right, the statistic of the contact discontinuity is completely resolved. In the following, the moments of the different quantities will not be presented anymore: the information given by those will be implicitly contained in the std and pdfs results.

3.0.6 Stochastic Richtmyer-Meshkov problem, axisymmetric geometry

We are now interested in the 2-D space Richtmyer-Meshkov problem. A shock propagating in a fluid hits an non moving interface between a light and a heavy fluid. When this interface is perturbed, hydrodynamical instabilities are developing. The perturbation of the interface, for this first 2-D RM problem, is modeled by a random variable translating the interface on the x axe. The initial conditions are

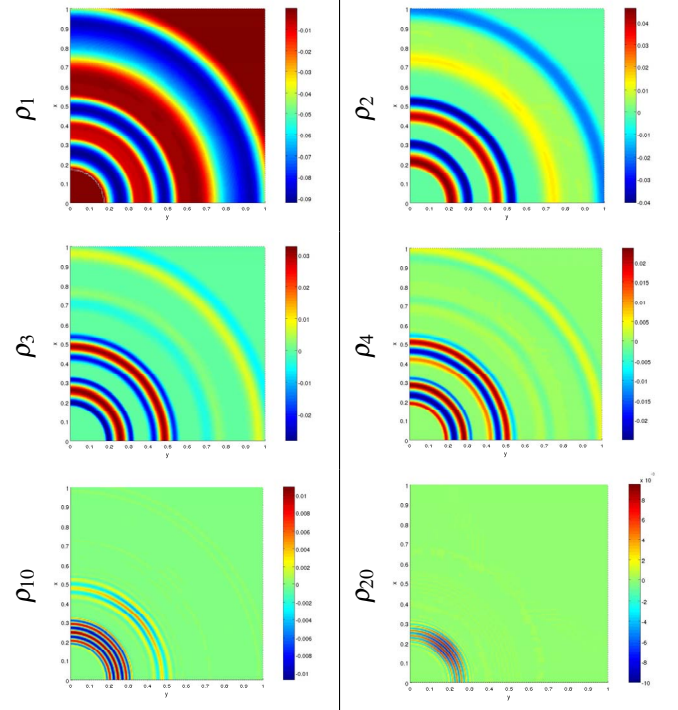Polynomial Moments of mass density ρ at $t = 0.24$

FIGURE 8. Stochastic Riemann problem with initial conditions given by (34). We show the moments of orders $1, 2, 3, 4, 10$ and 20 of the mass density ρ at time $t = 0.24$. The more the order is high, the finer is the information brought to the statistic of the flow: the rarefaction fan is resolved accurately for low orders. For example, moment ρ_{10} do not contribute to the rarefaction fan statistic whereas the modes in the vicinity of the shocks and interface are still represented until ρ_{20}. Note that once again, the interface and the shock have different behaviours (as in figure 3 and its explanation) as the interface needs lower orders for complete resolution.

given by

$$
\begin{cases}
\rho(x,y,0,\Xi) = \begin{cases} 4, & \text{if } r \leq r_{interface}(\Xi). \\ 1, & \text{if } r_{interface}(\Xi) \leq r \leq r_{shock}. \\ \dfrac{2\gamma - \gamma s + s}{2\gamma - \gamma s - s}, & \text{if } r \geq r_{shock}. \end{cases} \\[2em]
u(x,y,0,\Xi) = \begin{cases} 0, & \text{if } r \leq r_{interface}(\Xi). \\ 0, & \text{if } r_{interface}(\Xi) \leq r \leq r_{shock}. \\ -\dfrac{1}{2}\sqrt{\dfrac{s(\rho-1)}{\rho(1-s)}}, & \text{if } r \geq r_{shock}. \end{cases} \\[2em]
v(x,y,0,\Xi) = \begin{cases} 0, & \text{if } r \leq r_{interface}(\Xi). \\ 0, & \text{if } r_{interface}(\Xi) \leq r \leq r_{shock}. \\ -\dfrac{1}{2}\sqrt{\dfrac{s(\rho-1)}{\rho(1-s)}}, & \text{if } r \geq r_{shock}. \end{cases} \\[2em]
p(x,y,0,\Xi) = \begin{cases} 1, & \text{if } r \leq r_{interface}(\Xi). \\ 1, & \text{if } r_{interface}(\Xi) \leq r \leq r_{shock}. \\ \dfrac{1}{1-s}, & \text{if } r \geq r_{shock}. \end{cases}
\end{cases}
\tag{35}
$$

11

A shock is initialized at $r_{shock} = 0.7$ in the light fluid. For $t > 0$ the shock propagates in the direction of the uncertain interface. The coefficient s deontes the strength of the shock and is taken $s = 0.5$ with $\gamma = 1.4$ in the simulations. The uncertainty on the initial interface position is modeled by a random variable

$$r_{interface}(\Xi) = 0.5 + 0.1\Xi,$$

where Ξ is an uniform random variable on $[-1, 1]$. Note that the boundary conditions are the same as precedently (section 3.0.5).

Time evolution of the mean of the mass density ρ

FIGURE 10. 2-D Richtmyer-Meshkov problem with initial conditions given by (35). The figures show the time evolution of the mean of the mass density with respect to x and y. As soon as $t > 0$, the light fluid in amont of the shock refects against the left and bottom walls. The fluid is then compressed in the bottom left quarter of the domain, on the diagonal of this quarter (cf. figure 9 bottom right).
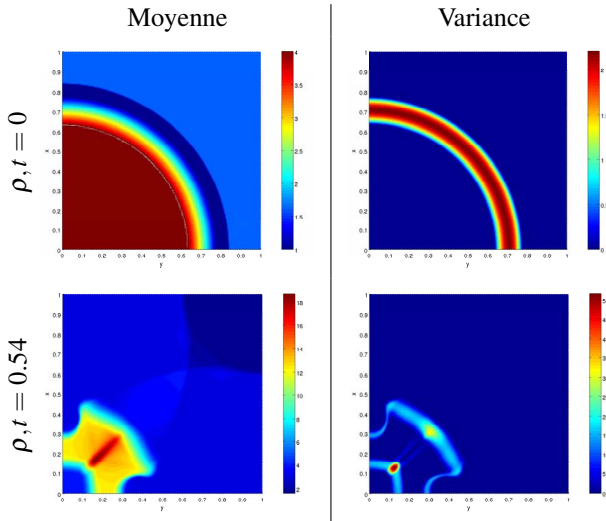
FIGURE 9. 2-D Richtmyer-Meshkov problem with initial conditions given by (35). The left column shows the means and std of the mass density at $t = 0$ and $t = 0.54$, the right column shows the std of ρ at times $t = 0$ and $t = 0.54$. The computation has 200×200 cells, $P = 20$. A level 7 in the 1-D Clenshaw-Curtis rule is used for numerical integration.

Figure 9 shows the means and std of the mass density at times $t = 0$ and $t = 0.54$: the wall boundary conditions at the bottom and left and the non zero initial components of the velocity explain the loss of the radial symmetry. Figure 10 shows the time evolution of the mean of the mass density and help understand the geometry of the flow: initially, the uncertainty is carried by the mass density only (velocity and pressure are constant through the interface) Two phenomena must be taken into account in order to explain the final time geometry. These are more easily observable on figure 10. The first consists in the reflection of the light fluid against the wall boundaries in amont of the shock. This happens as soon as $t > 0$. The wall boundaries then foster a compression of the fluids along the first diagonal of the domain . The second phenomenon concerns the interaction shock-interface, see the diagonal of the simulation domain
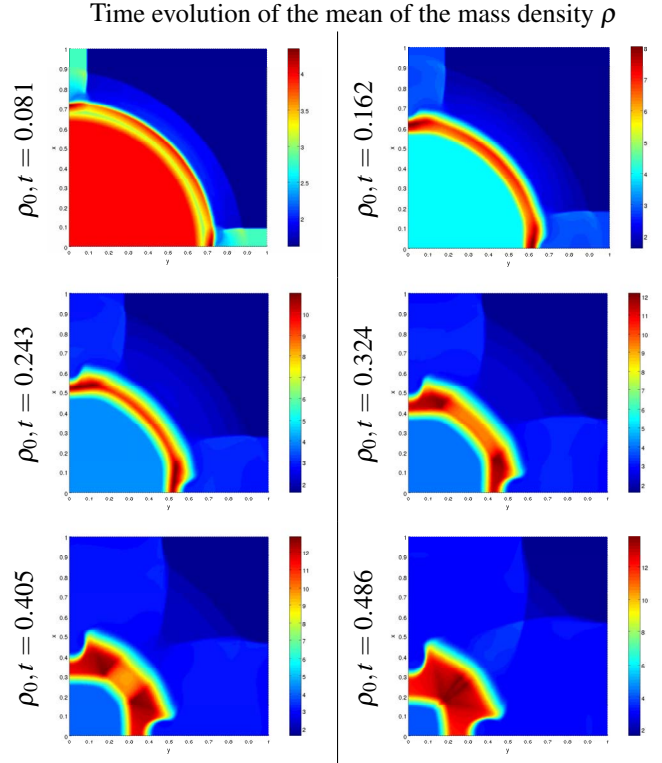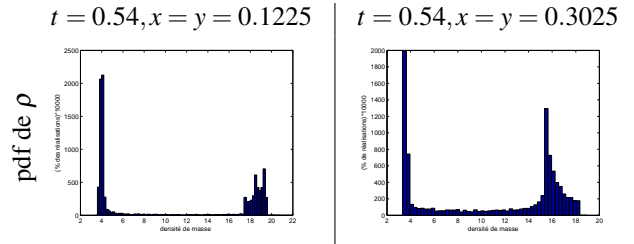

FIGURE 11. 2-D Richtmyer-Meshkov problem with initial conditions given by (35). The figure shows the pdfs of the mass density at two space locations, $x = y = 0.1225$ (left) and $x = y = 0.3025$ (right), at time $t = 0.54$. The pdfs are extracted from the same computation as those of figure 9. For these two space positions, two modes are identifiable corresponding to the floors of the transmitted shock (left), and of the interface (right).

where the shock wave hits the uncertain interface. This results in three distinct aves linked to the three waves of the deterministic system (transmitted shock, interface, reflected shock). At final

12

time, figure 9, the transmitted shock (in the heavy fluid) reflected against the wall boundaries but has not yet gone through the interface. The mean mass density is more important in the bottom left quarter of the domain, in particular on its diagonal.

For this test case, at final time, the uncertainty is concentrated at two locations of the simulation domain, in the area of important mass density: the most uncertain point (more important std), near the origin is in the variability area of the transmitted shock interacting with the shocks coming from the wall boundaries. The second most uncertain point is located on the interface: the increase of the std with time is due to the compression through the shock.

Figure 14 shows the pdfs of the mass density at space location $x = y = 0.1225$ (left), in the variability area of the transmitted shock and at $x = y = 0.3025$ (right), in the variability area of the interface. For both picture, two modes appears corresponding to the probable floors of the shock and contact discontinuity. For this test-case, for one realization of the random variable 'interface", the floors on each side of the discontinuities are not constant: the spreading of the modes is physical.

The precedent test-cases[27] emphasize the fact that the nature of the random variables of the different quantities can change a lot with the time and locations in space. Let's consider the mass density: in the vicinity of discontinuities, the pdfs of the random variables $\rho(x,y,t,\Xi)$ for fixed x,y,t present two modes[28] (cf. figures 7 and 14) testifying of the fact that $\rho(x,y,t,\Xi)$ tensd toward a discrete random variable[29]. At other space locations, the pdfs of the same quantity can be smoother and $\rho(x,y,t,\Xi)$ is a continuous random variable.

3.1 Combination of the Riemann Problem and the RM problem

The following problem combines the two precedent: it consists in an uncertain Riemann problem considered for later times than for problem of section 3.0.5. For early times, the problem behaves exactly as the stochastic Riemann problem precedently presented: an uncertain shock, an uncertain interface and an uncertain rarefaction fan appear in the different fluids. For later times, the uncertain shock focuses at the center of the domain where it reaches wall type boundary conditions: the reflected uncertain shock goes back toward the perturbed interface and goes through it, which is presicely the configuration precedently presented (see section 3.0.6). As the uncertain shock hits the uncertain interface, interface instabilities grows as the light fluid pushes the heavy fluid.

Furthermore, for this last problem, we consider the uncertain initial interface position is no longer modeled by a random variable but by a stochastic process represented by its Karuhnen-

Loève development, see [29, 21, 5]. In this paper, we consider the particular stochastic process[30]: $(F_\beta)_{\beta \in [0, \frac{\pi}{2}]}$ of mean μ, variance σ with covariance kernel

$$K(\beta, \zeta) = e^{-\frac{c}{L}|\beta - \zeta|}, \qquad (36)$$

where[31] $L = \frac{\pi}{2}$ is the length of the simulation domain such that its KL expansion is given by

$$F_\beta = \mu + \sigma \sum_{n=1}^{\infty} \Xi_n \sqrt{\lambda_n} g_n(\beta), \qquad (37)$$

where where the basis $(\Xi_n^i)_{i \in \{1,2\}, n \in \mathbb{N}}$ are uniform random variables **i**ndependent and **i**dentically **d**istributed (i.i.d.) (same choice as in [36] for example). The $(\lambda_i, g_i)_{i \in \mathbb{N}}$ are the eigenvalues and eigenvectors of the kernel (36): such a choice of kernel enables dealing with quasi-analytical expressions of the eigenvalues and eigenvectors. Theses expressions are not recalled in this paper, for more details see [28]. The correlation length is denoted by $L_{corr} = \frac{L}{c}$. The covariance kernel (36) is homogeneous, $K(\beta, \zeta) = \widetilde{K}(\beta - \zeta)$. The behaviour of the the growth rate between two points directly depends on L_{corr}. In practice, we need to truncate the expansion (37):

$$F_\beta(\omega) \approx F_\beta^Q(\omega) = \mu + \sigma \sum_{n=1}^{Q} \Xi_n(\omega) \sqrt{\lambda_n} g_n(\beta). \qquad (38)$$

The truncature order of the KL expansion is noted Q. It also corresponds to the stochastic dimension.

We now consider an interface initially represented by the stochastic process (38) with correlation length given by $\frac{L}{c} \approx \frac{1.5708}{5} \approx 0.3142$. Figure 12 (left) shows the decrease of the eigenvalues of F_β^K for $L_{corr} = 0.31$ with respect to the truncature order Q: every modes of order lower than 10 are influent on the development of F_β^K. Figure 12 (right) shows 30 paths of the process for $Q = 5$, i.e. $F_\beta^5 - \mu$: each curve represents one (normalized) path of the interface on $[0, \frac{\pi}{2}]$.

Figure 13 presents the means and variances of the mass density for $Q = 5$ at several times. The solutions for $t > 0$ present several differences in comparison with the precedent simulation of section 3.0.5 testifying of the sensitivity of the solutions to the interface perturbations: at time $t = 0.185$, for figure 13 (middle), the rarefaction fan presents three areas of strong variability. These areas are more localized, less spread out for the second

---

[27]initial conditions (34) and (35) and figures 6-8-7 and 9-10-14.
[28]Two Dirac masses corresponding to the floors of the shock and interface.
[29]or piecewise continuous as the floors are not constant, cf. [30].

[30]A more complete study of this kind of initialization will be tackled in further publications.
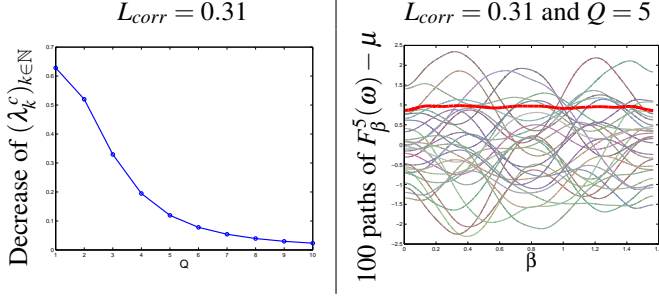[31]quarter of circle.

FIGURE 12. The parameter $L_{corr} = 0.31$ is fixed. The process is centered with $\beta \in [0, \frac{\pi}{2}]$. Left: decrease of the eigenvalues of the kernel (36). Right: paths of the centered process and std (thick curve).

figure. The other waves are also affected: the variability areas in the vicinity of the shock wave have an axial symmetry with respect to the first bissectrice. The uncertainty on the interface is less important than on the rarefaction fan or the shock, see figure 13 (middle): this is also the case at final time, on figure 13 (bottom). At final time, figure 13, three realizations of the interface positions are displayed: these show that finer scales are taken into account through the uncertainty propagation methods.

The sensitivity of the system to small hydrodynamical instabilities do not explain the complete behaviour of the solution of figure 13: we are here experimenting the curse of dimensionality, i.e. more stochastic dimensions are needed in order to accurately represent the initial perturbed interface. On a uncertainty propagation point of view, this implies an explosion of the number of polynomial moments and size of the system to solve: this problem will be dealt with in further publications; in particular, we will resort sparse quadratures in order to integrate the hessian of the entropy during the computations.

Let's now tackle the statistics of the mass density in the vicinity of the interface for the final time, $t = 0.74$. Figure 14 (left) shows the pdfs of the mass density at the same time, $t = 0.74$, and the same space locations, $x = y = 0.3525$ for simulations of sections 3.0.5 and 3.1 while figure 14 (right) shows a cut along the first bissectrice ($\beta = \frac{\pi}{4}$) of one realization of the random variable $\rho(r, \frac{\pi}{4}, 0.74, \Xi)$. For the reference solution (figure 14 (top) corresponding to $L_{corr} = \infty$), the rv $\rho(x, y, t, \Xi)$ behaves like a mixed discrete/continuous rv in the vicinity of the interface position: indeed, the pdf shows one Dirac mass near $\rho \approx 0.85$ and has a continuous behaviour for $1.25 \leq \rho \leq 1.45$. For the realization of the rv of figure 15 ($L_{corr} = \infty$), the interface position is at $r \approx 0.3$: on the left of the discontinuity, the solution has a floor (corresponding to the Dirac mass of the pdf). On the right side of the discontinuity, the solution presents some steep variation with respect to r explaining the right hand side of the pdf (figure 14 $L_{corr} = \infty$).

For the other correlation length ($L_{corr} = 0.31$), the flow behaves differently: figure 14 (bottom) are very different from the
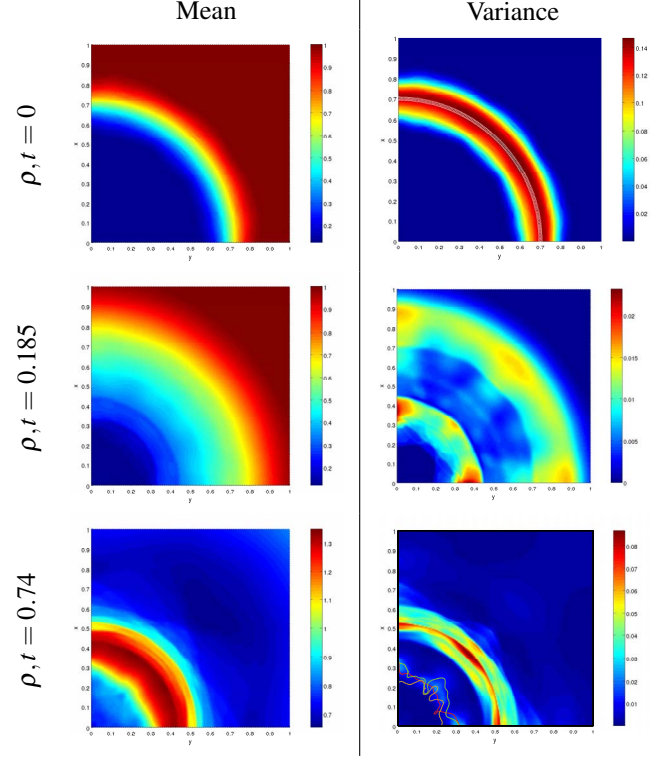

FIGURE 13. Stochastic Riemann Problem. The figure shows the means and variances of the mass density at several times $t = 0$, $t = 0.185$ and $t = 0.74$ (spatial distributions). The interface is uncertain, represented by a KL expansion with $L_{corr} = 0.31$, $P = 2$, $Q = 5$, $\sigma = 0.08$.

top ones as the pdf seems to behave more continuously. This phenomena is explained by the presence of finer and finer scales giving birth to more complex patterns in the realizations of the interface positions: for finite correlation lengths, at final time $t = 0.74$, hydrodynamical instabilities are developing for every realizations of the rv; these fluid instabilities are interacting with each other leading to shock reflections/transmissions in the transverse direction to r affecting the mass density profiles in the radial direction (figure 15).

Figure 15 shows four cuts along the first bissectrive of realizations of the random variable $\rho(x, y, 0.74, \Xi)$: the hydrodynamical instabilities are occuring at $t = 0.74$ which affects the pdf of the mass density $x = y = 0.3525$. Shock reflections lead to the loss of the Dirac mass around $\rho = 0.85$, replaced by several equiprobable values for $0.7 \leq \rho \leq 1.1$. These are illustrated on figure 15 by several oscillations occuring on the left side of the discontinuity. The same phenomena affects the pdfs/realizations of figures 14 – 15 for the lower correlation length ($L_{corr} = 0.31$) leading to continuous like behaviours of the pdfs/realizations in figures 14/15.

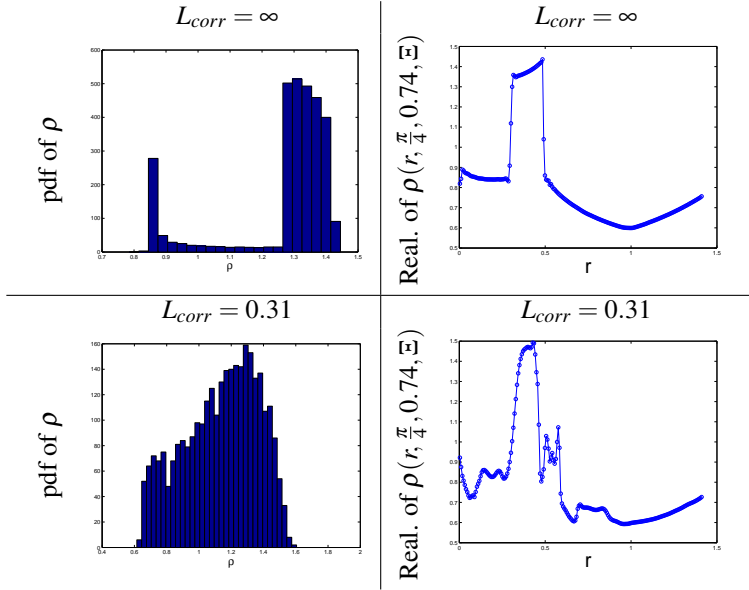The latter simulations tend to show the great sensitivity of

FIGURE 14. Left: pdfs of the mass density (2000 samples) in the vicinity of the interface, at the same space location $x = y = 0.3525$, for the precedent simulations at time $t = 0.74$ (the reference one, $L_{corr} = \infty$, correspond to the Riemann problem of section 3.0.5). Right: one realization of the rv $\rho(x, y, t, \Xi)$ along the first bissectrice ($\beta = \frac{\pi}{4}$) in function of the radius for the four precedent simulations at time $t = 0.74$ for both problems.
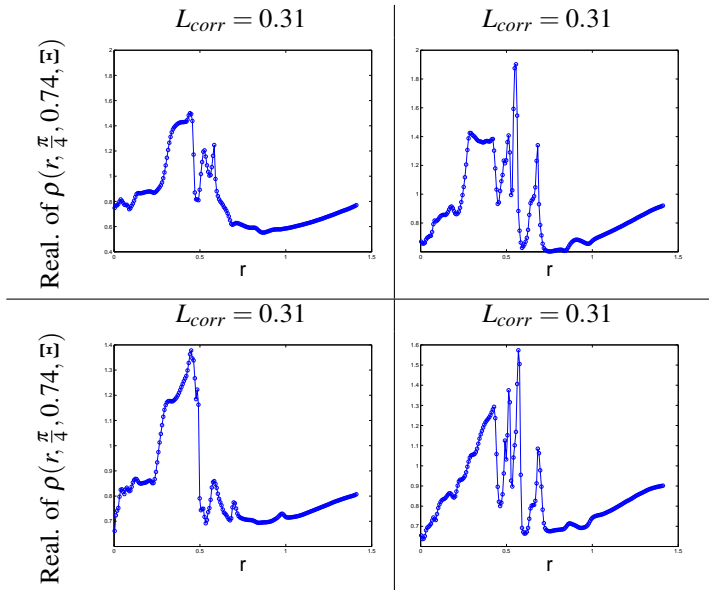

FIGURE 15. Four realizations of the rv $\rho(x, y, t, \Xi)$ along the first bissectrice ($\beta = \frac{\pi}{4}$) in function of the radius for the four precedent simulations at time $t = 0.74$.

the flow with respect to the different scales: the finer the modes of the stochastic process, the larger the size of the variance in the vicinity of the interface (cf. figure 13 (bottom right) with the amplitudes of the realizations of the hydrodynamical instabilities). These results remind some of the features of transition of incompressible fluids toward turbulence. This study constitutes a first step in the investigation of this discipline through stochastic modeling *via* Polynomial Chaos. A lot of work remains to be done in this area: one would for example like to link the size of the variability zone of the interface to the size of the turbulent mixing zone of the fluids, or understand how the size of this zone behaves with respect to the covariance kernel and the other parameters of the initialization. A deeper study of the IPMM model for transition toward turbulence remains in the field of investigation and will be tackle in further publications as we here focused on the uncertainty propagation method.

4 Conclusion

In this paper, we were interested in several uncertain shock tubes. We have first studied the Sod shock tube (Riemann problem) then a Richtmyer-Meshkov problem and a combination of both for the last simulation. We have proposed a numerical method to propagate the uncertainty in the initial interface position through a 2D Euler system. Finally, we have put forward the effects of nonlinearities with respect to uncertainty: the area of highest variability can be very localized with an explosion of the uncertainty at some specific points of the simulation domain (see section 3.0.4) or very spread out (see section 3.1) on the whole domain with different behaviours (discrete or continuous random variables) according to the kind of wave considered (shock, interface, rarefaction).

The stochastic interface has been treated as random variable first, then as a stochastic process. For the last simulation, a Karhunen-Loève (spectral) development has been evaluated for representing several the stochastic process with exponential kernel. The KL development provides a powerful tool for stochastic process representation thanks to linear combinaison of random variables. A deeper study of initializations through stochastic processes is under investigation and will be the point of further publications.

An Intrusive Polynomial Chaos method has been studied and applied in several stochastic dimensions so as to propagate the uncertainty on the initially pertubed interface position. The approach reveals to be very robust and stable under some simple conditions. This paper shows that these conditions can be easily satisfied using fully tensorized quadrature rules.

On a physical point of view, the simulations of this paper have emphasized the importance of the transversal effects on the statistics of the interface position and the great sensitivity of the flow with respect to the uncertain interface: the study of the influence of finer and finer modes in the perturbation of the interface

15

through KL development is also under study and will be tackled in further publications.

REFERENCES

[1] R. Abgrall. A Simple, Flexible and Generic Deterministic Approach to Uncertainty Quantifications in Non Linear Problems: Application to Fluid Flow Problems. *Rapport de Recherche INRIA*, 2007.

[2] S. Acharjee and N. Zabaras. Uncertainty Propagation in Finite Deformations - A Spectral Stochastic Lagrangian Approach. *Comp. Meth. Appl. Mech. Engrg.*, 195:2289–2312, 2006.

[3] R.H. Cameron and W.T. Martin. The Orthogonal Development of Non-Linear Functionals in Series of Fourier-Hermite Functionals. *Annals of Math.*, 48:385–392, 1947.

[4] J.-C. Chassaing and D. Lucor. Stochastic investigation of flows about airfoils at transonic speeds. *AIAA J.*, 48(5):in press, May 2010.

[5] C.-H. Su D. Lucor and G.E. Karniadakis. Karhunen-loève representation of periodic second-order autoregressive processes. In G.D. van Albada M. Bubak and P.M.A. Sloot, editors, *Lecture Notes in Computer Science*, volume 3038, pages 827–834, Heidelberg, 2004. Springer-Verlag.

[6] R. Eymard, T. Gallouet, and R. Herbin. *Finite Volume Methods, in Handbook of Numerical Analysis*, volume 7. P.G. Ciarlet, J. L. Lions eds, 2006.

[7] M. Gerritsma, P. Vos, J.-B. van der Steen, and G. Karniadakis. Time Dependent generalized Polynomial Chaos. *Preprint*, 2009.

[8] R.G. Ghanem and P. Spanos. *Stochastic Finite Elements: a Spectral Approach*. Springer-Verlag, 1991.

[9] H. Jourdren and S. Del Pino. Arbitrary High-Order Schemes for the Linear Advection and Wave Equations: Application to Hydrodynamics and Aeroacoustics. *C.R. Acad. Sci. paris, Ser. I*, 342:441–446, 2006.

[10] Michael Junk. Maximum Entropy for Reduced Moment Problems. *Math. Mod. Meth. Appl. Sci.*

[11] J. Ko. *Application des Polynômes de Chaos Généralisés à la Simulation d'Écoulements Cisaillés Stochastiques*. Ph. d. thesis, Thèse de doctorat de l'UPMC, Institut Jean Le Rond d'Alembert, Paris VI, 2009.

[12] E. Leinov, G. Malamud, Y. Elbaz, L.A. Levin, G. Ben-Dor, D. Shvarts, and O. Sadot. Experimental and Numerical Investigation of the Richtmyer-Meshkov Instability under Re-Shock Conditions. *J. Fluid Mech.*, 626:449–475, 2009.

[13] J. Lindl. The Evolution toward Indirect Drive and Two Decades of Progress toward ICF Ignition and Burn. In *11th International Workshop on Laser Interaction and Related Plasma Phenomena*, 1993.

[14] D. Lucor, C. Enaux, H. Jourdren, and P. Sagaut. Multi-Physics Stochastic Design Optimization: Application to Reacting Flows and Detonation. *Comp. Meth. Appl. Mech. Eng.*, 196:5047–5062, 2007.

[15] D. Lucor, J. Meyers, and P. Sagaut. Sensitivity Analysis of LES to Subgrid-Scale-Model Parametric Uncertainty using Polynomial Chaos. *J. Fluid Mech.*, 585:255–279, 2007.

[16] O. P. Le Maître and O. M. Knio. Uncertainty Propagation using Wiener-Haar Expansions. *J. Comp. Phys.*, 197:28–57, 2004.

[17] O. P. Le Maître and O. M. Knio. A Stochastic Particle-Mesh Scheme for Uncertainty Propagation in Vortical Flows. *J. Comp. Phys.*, 226:645–671, 2007.

[18] L. R. Mead and N. Papanicolaou. Maximum Entropy in the Problem of Moments. *J. Math. Phys.*, 25 (8), 1984.

[19] I. Müller and T. Ruggeri. *Rational Extended Thermodynamics, 2nd ed.* Springer. Tracts in Natural Philosophy, Volume 37, 1998. Springer-Verlag, New York.

[20] H. N. Najm O.P. Le Maître, O. M. Knio and R. G. Ghanem. A Stochastic Projection Method for Fluid Flow I: Basic Formulation. *J. Comp. Phys.*, 173:481–511, 2001.

[21] K.K. Phoon, S.P. Huang, and S.T. Quek. Implementation of Karhunen-Loeve expansion for simulation using a wavelet-Galerkin scheme. *Prob. Eng. Mech.*, 17:293–303, 2002.

[22] G. Poëtte. *Propagation d'Incertitudes pour les Systèmes de Lois de Conservation, Méthodes Spectrales Stochastiques*. Phd thesis, Université Pierre et Marie Curie, Institut Jean Le Rond D'Alembert, 2009.

[23] G. Poëtte, B. Després, and D. Lucor. Uncertainty Quantification for Systems of Conservation Laws. *J. Comp. Phys.*, 228(7):2443–2467, 2009.

[24] G. Poëtte, D. Lucor, and B. Després. Uncertainty Propagation for Systems of Conservation Laws, High-Order Stochastic Spectral Methods. In Springer, editor, *International Conference On Spectral Analysis and High Order Methods*, 2009.

[25] D. Serre. *Systèmes Hyperboliques de Lois de Conservation, partie I*. Diderot, 1996. Paris.

[26] D. Serre. *Systèmes Hyperboliques de Lois de Conservation, partie II*. Diderot, 1996. Paris.

[27] F. Simon, P. Guillen, P. Sagaut, and D. Lucor. A gPC based approach to uncertain transonic aerodynamics. *CMAME*, 199:1091–1099, 2010.

[28] P. Spanos and R. G. Ghanem. Stochastic Finite Element Expansion for Random Media. *ASCE J. Eng. Mech.*, 115(5):1035–1053, 1989.

[29] R. A. Todor and C. Schwab. Karhunen-Loève approximation of random fields by generalized fast multipole methods. *J. Comp. Phys.*, 217(1):100–122, 2006.

[30] E.F. Toro. *Riemann solver and numerical methods for fluid dynamics*. Springer-Verlag, 1997.

[31] P. Vos. Time dependent polynomial chaos. Master of science thesis, Delft University of technology, Faculty of Aerospace engineering, 2006.

[32] X. Wan and G. E. Karniadakis. Stochastic Heat Transfer Enhancement in a Grooved Channel. *J. Fluid Mech.*, 565:255–278, 2006.

[33] X. Wan and G.E. Karniadakis. Beyond Wiener-Askey Expansions: Handling Arbitrary PDFs. *SIAM J. Sci. Comp.*, 27(1-3), 2006.

[34] X. Wan and G.E. Karniadakis. Multi-Element generalized Polynomial Chaos for Arbitrary Probability Measures. *SIAM J. Sci. Comp.*, 28(3):901–928, 2006.

[35] N. Wiener. The Homogeneous Chaos. *Amer. J. Math.*, 60:897–936, 1938.

[36] D. Xiu and J.S. Hesthaven. High-Order Collocation Methods for Differential Equations with Random Inputs. *J. Sci. Comput.*, 27(3):1118–1139, 2005.

[37] D. Xiu and G.E. Karniadakis. The Wiener-Askey Polynomial Chaos for Stochastic Differential Equations. *SIAM J. Sci. Comp.*, 24:619–644, 2002.

[38] D. Xiu, D. Lucor, and G. E. Karniadakis. Stochastic Modeling of Flow-Structure Interactions. In *Computational Fluid and Solid Mechanics, Elsevier, Proceedings of the 1st MIT conference, Cambridge, Massachussetts, K.J. Bathe (Ed.)*, volume 2, pages 1420–1423, 2001.